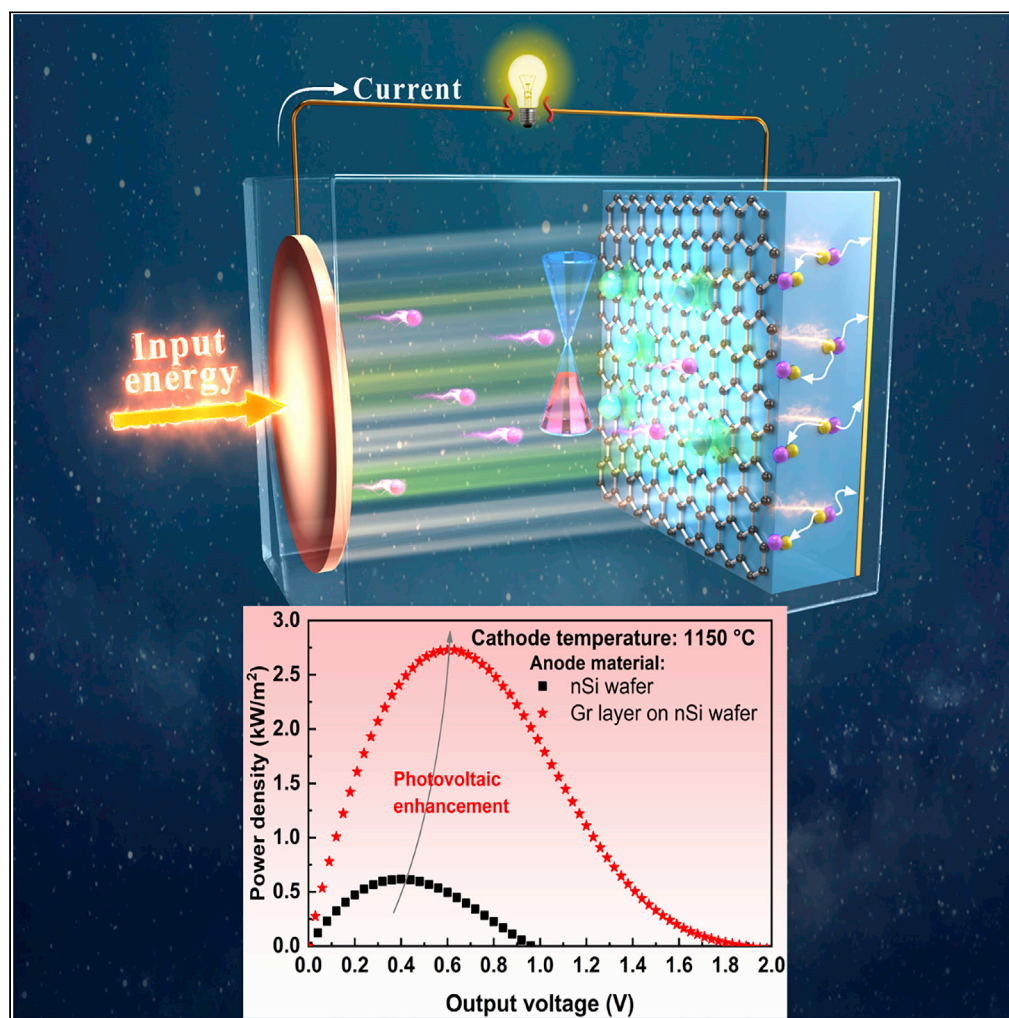Article

Hybrid thermionic-photovoltaic converter with graphene-on-semiconductor heterojunction anode for efficient electricity generation

Hao Qiu, Shisheng Lin, Haoran Xu, Guanghui Hao, Gang Xiao

xiaogangtianmen@zju.edu.cn

Highlights

A novel thermionic energy converter is originally proposed and measured

Open-circuit voltage is increased from 0.9 to 1.9 V by the photovoltaic effect

A power density of 2.7 kW/m² with an electronic efficiency of ∼27% is measured

Ultralow work function is obtained by forming barium surface dipoles

Article

Hybrid thermionic-photovoltaic converter with graphene-on-semiconductor heterojunction anode for efficient electricity generation

Hao Qiu,[1] Shisheng Lin,[2] Haoran Xu,[1] Guanghui Hao,[3] and Gang Xiao[1,4,*]

SUMMARY

Thermionic energy converters are solid-state heat engines to produce electricity with significant potential, whereas the output voltage is constrained by the work function difference between cathode and anode. In this work, we originally apply a graphene-on-semiconductor heterojunction anode to a thermionic-photovoltaic (TIPV) converter to output additional voltage. Thermionic electrons are injected into the graphene layer and then recombined with photogenerated holes. Photo-generated electrons are extracted from the conduction band and reinjected into the cathode through an external load. A proof-of-concept demonstration of the TIPV converter is developed with barium surface-engineered cathode and anode. Open-circuit voltage is increased from ~0.9 to ~1.9 V by comparing with an identical configuration without graphene layer. The TIPV converter yields a power generation density of 2.7 kW/m^2 with an electronic efficiency of ~27%. This work paves the way for the development of TIPV converter toward high power density.

INTRODUCTION

Thermionic (TI) energy converters can directly convert thermal energy to electrical power, with a prospect of power density of 1 MW/m^2 and efficiency of >30% (Campbell et al., 2021). TI converter can be applied to concentrated solar power (Schwede et al., 2013; Trucchi et al., 2018; Xiao et al., 2017), space nuclear power (Bennett et al., 1996; Deng et al., 2021), deep-space missions (Schwede et al., 2010), and other scenarios. A TI converter consists of a hot cathode and a cooler anode separated in parallel by a vacuum gap. A fraction of electrons in the cathode can absorb adequate heat to overcome the cathode work function and emit from the surface. After transit through the vacuum gap, a fraction of electrons is collected by the anode. The electrons can be extracted through an external circuit to generate electricity and reinject into the cathode.

High work function of practical electrode is a key factor that limits the performance of TI converters, and many efforts have been paid to obtain low work function materials. Low work function can be achieved by surface texturing, alkali or alkali-earth metal coating (e.g., Ba or Cs) (Schwede et al., 2010; Yuan et al., 2017), Cs/O activation (Yuan et al., 2015), and n-type doped hydrogen-terminated nanodiamond films (Koeck and Nemanich, 2017). In addition, lanthanum boride thin films on tantalum substrates can exhibit a work function of ~2.6 eV in the temperature range of 700°C–1600°C (Bellucci et al., 2019). A work function of 2.1 eV can be acquired by depositing a barium fluoride of 2 nm thickness on GaAs substrate (Serpente et al., 2020). The lowest work function reported so far is 0.67 eV of diamond-based materials (Koeck and Nemanich, 2017). Schwede et al., (2010) developed photon-enhanced thermionic emission (PETE) of p-type semiconductor cathode, which reduces the electron emission barrier by the difference between photo-induced electron's quasi-Fermi level and Fermi level, so that the output current density is enhanced. Very recently, Rahman and Nojeh (Rahman and Nojeh, 2021) proposed that the PETE mode could only operate under specific conditions. Otherwise, it still operates at pure thermionic mode.

Improvement of the output voltage of TI converters has also attracted much attention. Since a high cathode work function will seriously limit the TI current, an effective method is to reduce the anode work function. However, the bottleneck of obtaining ultralow work function limits further increase of the output voltage. Recently, surface photovoltage (SPV) effect of the anode and hybrid thermionic-photovoltaic (TIPV)

[1]State Key Laboratory of Clean Energy Utilization, Zhejiang University, 38 Zheda Road, Hangzhou 310027, China

[2]Department of Information Science & Electronic Engineering, Zhejiang University, Hangzhou 310027, China

[3]Cathode Engineering Center, Beijing Vacuum Electronics Research Institute, 13 Jiuxianqiao Road, Beijing 100015, China

[4]Lead contact

*Correspondence: xiaogangtianmen@zju.edu.cn

https://doi.org/10.1016/j.isci.2022.105051

architecture were proposed (Schindler et al., 2019; Datas and Vaillon, 2019b). Their common feature is that anode utilizes both photons and electrons. SPV effect refers to photon-generated electron-hole pairs near surface in an n-type semiconductor, which can increase its Fermi level and thus lower the work function, whereas it is opposite in a p-type semiconductor. Schindler et al., (2019) measured a TI converter with a Ba-activated n-type GaAs anode and it reduced the anode work function from 2.08 eV to 1.80 eV by inducing an SPV with illumination. For Cs/O_2-activated n-type GaAs, an ultralow work function of 0.70 eV was reached by inducing an SPV.

TIPV converter applies a photovoltaic (PV) cell connected to anode of the TI converter. The PV cell absorbs both photons and electrons radiated from the cathode and obtains a voltage increment (Datas and Vaillon, 2019a). Bellucci et al. (2020) constructed a TIPV prototype using a p/n GaAs PV anode, and consequently obtained a voltage boost of ~1 V and a power output density of ~1 $\mu W/cm^2$ at a cathode temperature of ~1340°C. It is worth noting that the anode surface should be a hole-selective, i.e. p-type doped, in TIPV converters and the unexpected SPV effect will increase the anode work function. Very recently, Bellucci et al. (2022a) developed a three-terminal TIPV converter, where TI current and PV current were collected independently, and obtained a huge power capacity enhancement, from 0.35 mW to 125.96 mW when operating at 1400°C.

In addition, anode with graphene (Gr) layer attracted attention due to superior optical and electronic properties. Yuan et al., (2017) lowered the graphene work function to ~1.25 eV by lowering vacuum level with Cs/O surface coating, and further reached 1.01 eV by upshifting Fermi level with electrostatic gating. They applied a graphene anode with both barium coating and electrostatic gating to a TI converter (Yuan et al., 2015). But maintaining an electric field consumes extra energy, making it unfeasible in practical applications. Graphene-on-semiconductor PV cells have achieved rapid development due to its superiority, which can be applied to both solar cells and thermophotovoltaics (Kong et al., 2019; Lin et al., 2016). So far, graphene-on-semiconductor PV cells have not been applied to TI converters as anode to improve the output voltage and thus the power density.

In this work, we propose for the first time a TIPV converter with a graphene-on-semiconductor heterojunction anode and report the first proof-of-concept demonstration of a TIPV prototype comprising a dispenser cathode and a barium-coated graphene-on-silicon heterojunction anode. The unexpected SPV effect of p-type III-V semiconductor in typical TIPV converters is eliminated by using n-type semiconductor as the substrate of the heterojunction. The converter can also take the merits of graphene-on-silicon PV cell. Both the cathode and the anode obtain low work function by forming Ba dipoles. We demonstrate significant boosts of both open-circuit voltage and power output by comparing with an identical configuration without graphene layer. A xenon lamp illumination is further applied to increase the injected photons on the anode, and thus improves the power output. In addition, space charge effect between electrode gaps is analyzed in detail.

Concept and working principle

A TIPV converter with a graphene-on-semiconductor heterojunction anode contains two physical processes connected in series by electrons, i.e., TI process and PV process, as shown in Figure 1. In the TI process, cathode electrons absorb enough heat to overcome the cathode work function Φ_C, and then emit toward an anode surface. The emitted electrons with energy that can overcome the highest barrier between electrodes will be collected by the graphene layer. The collected electrons thermalize to the Fermi level of anode surface rapidly. In the PV process, the graphene-on-semiconductor heterojunction anode works as a PV cell. The semiconductor layer absorbs thermal photons from the cathode, and then generates electron-hole pairs. The electron-hole pairs are separated by a built-in electric field created by Schottky barrier. The photogenerated holes flow toward graphene layer and recombine with the collected electrons. On the meantime, the photogenerated electrons are extracted to external load from the conduction band of semiconductor, and then reinjected into the cathode, completing an "electronic cycle". This working principle can be viewed as a combined cycle of thermionic and photovoltaic in series with electrons as the working fluid.

RESULTS AND DISCUSSION

A TIPV converter and a measurement system were developed in this work (see Figure 2). A dispenser cathode was manufactured, in which a porous tungsten matrix was impregnated with barium-calcium
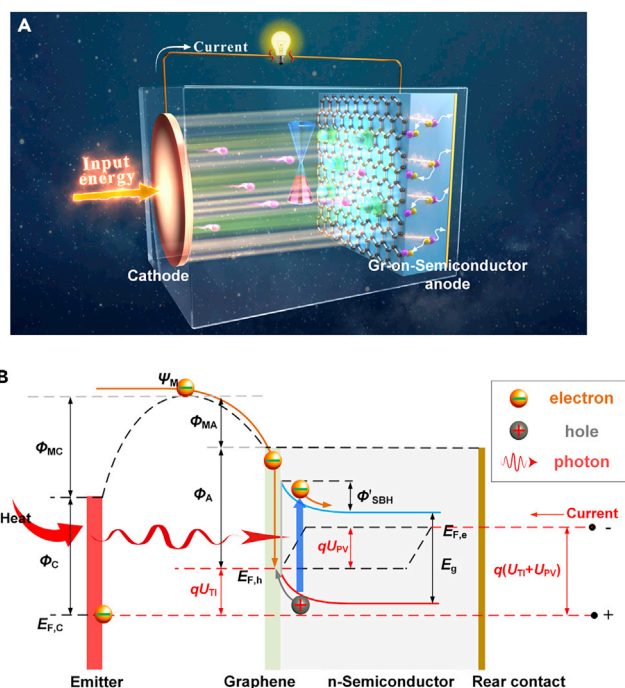
Figure 1. Schematic of TIPV converter with a graphene-on-semiconductor anode

(A) Structure Schematic.

(B) Energy-band diagrams. Here, Φ_C and Φ_A are the work functions of the cathode and the anode, respectively. ψ_M is the maximum electron barrier in the electrode gap. $E_{F,C}$ is the Fermi level of the cathode. $E_{F,e}$ and $E_{F,h}$ are the semiconductor quasi-Fermi levels of electron and hole, respectively, induced by photon illumination. $E_{F,h}$ equals to the Fermi level of the anode surface. E_g is the bandgap of the semiconductor. Φ'_{SBH} is the Schottky barrier height biased by the output voltage. U_{TI} and U_{PV} are the output voltage contributed by the TI process and the PV process, respectively.

aluminate as active materials. Alkali-earth metals, such as Ba and Cs atomics, adsorbed on the graphene, metal, and semiconductor surfaces can form dipoles, which will effectively reduce the work function (Sun et al., 2015; Yuan et al., 2017). In the dispenser cathode, the barium-calcium aluminate will chemically react with the tungsten matrix and continuously generate active Ba and BaO as the temperature increases. Ba and BaO begin to diffuse to the cathode surface at temperatures above 900°C, which reduces the work function by forming surface dipoles (Forman, 1976). Figure S1 gives the characterization of X-ray diffraction and scanning electron microscopy (SEM) for the barium-calcium aluminate, which indicates the composition is mainly $Ba_3CaAl_2O_7$. Figure S2 shows the SEM and energy dispersive spectra (EDS) of the emitting surface of the dispenser cathode after activation. It can be observed from the SEM image that the osmium film exhibits a porous skeleton structure. The pores in the osmium skeleton are filled with granular agglomerates, which are substances such as Ba, Al, and Ca. The Ba atomic percentage measures 1.22% according to the EDS. These Ba atoms form dipoles on the surface, and thus reduce the cathode work function.

A chemical vapor deposition (CVD)-grown monolayer graphene was transferred to an n-type silicon wafer substrate, forming a Schottky junction at the interface. The graphene/silicon Schottky junction was used as the anode of the TIPV converter. In addition, a pure thermionic converter with a bare n-type silicon wafer anode was also measured for comparison. The gap size between the cathode and the anode was set to be about 30 μm for all reported measurements, except where otherwise noted. As reported in the literature, in this case, part of the Ba atoms emits from the cathode surface and reaches the anode surface after passing through the vacuum gap (Yuan et al., 2017; Schindler et al., 2019). Thus, surface dipole also gradually forms on the anode and lowers the anode work function. In the experiment, the cathode was firstly heated to 900°C for ~2 h to stabilize the work functions of the cathode and the anode, and then specific experimental measurement was carried out. Details of experiment and sample preparation can be found in the STAR Methods section and Figures S1–S3.
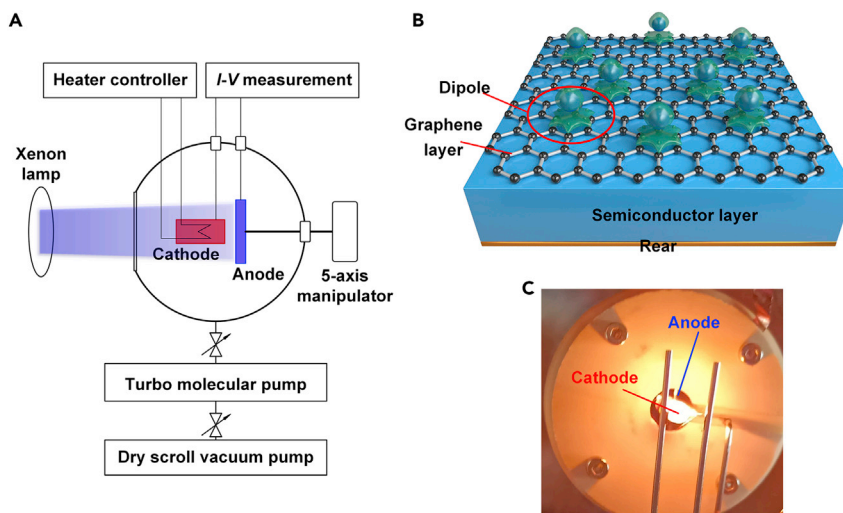
Figure 2. Schematics of the experimental system
(A) Schematic of the system, (B) schematic of a graphene-on-semiconductor anode with barium-induced dipoles, and (C) photograph of a TIPV converter. The anode area is ∼7-fold larger than that of the cathode.

Figure 3 shows the current density-voltage (*J-U*) and power density-voltage (*P-U*) characteristics of the TIPV and the TI converters at different cathode temperatures, respectively. An output voltage enhancement of ∼1 V is observed, which is contributed by photons from the cathode. As shown in Figure 3B, the maximum output power density is enhanced from 55.7 to 212.8 mW/cm^2 at the cathode temperature T_c of 1125°C. To our knowledge, this is the first demonstration of graphene-on-semiconductor PV cell working as the anode in a TIPV converter. A 2-terminal TIPV converter follows the constraint of current-match, that is TI current equals to PV current (Datas and Vaillon, 2019a). This means that the sub-converters may be biased to deviate from their respective maximum power points (MPPs) automatically. The dispenser cathode can emit a larger current due to a relatively low work function, whereas the relatively low cathode temperature leads to a lower PV current. The TI and the PV currents cannot match at their respective MPPs. To increase the PV current, a xenon lamp illumination is further applied to anode surface of the TIPV converter from the normal direction. The xenon lamp illumination is applied simply to bring the TIPV converter closer to MPP operating conditions for demonstration purposes. Consequently, the maximum output power density is further enhanced to 261.8 mW/cm^2. In practical applications, the PV current can be increased by increasing the cathode temperature, designing cathode materials with higher emissivity, and selecting suitable bandgap semiconductor to form the anode heterojunction.

Note that the anode reverse current of the TI converter is 2–4 orders of magnitude larger than that of the TIPV converter on the same condition. As shown in Figure 3C, the net current density reduces to about −90 mA/cm^2 at 3 V voltage for the TI converter, implying a significant anode reverse current density. It demonstrates that the TI performance is penalized with the high anode reverse current except for the lack of PV effect. This may be caused by high effective Richardson constant A_A of n-type silicon, which is about 252 A/(cm^2·K^2) (Li et al., 2010). In addition, part of the cathode radiation is converted into chemical energy to enhance output voltage in a TIPV converter, whereas all radiative heat flux from the cathode to the anode is converted to anode thermal heat in a TI converter. Therefore, we speculate that the anode temperature of the TIPV converter is lower than that of the TI converter at a same cathode temperature. The lower anode temperature of the TIPV converter results in a lower reverse current density according to the Richardson-Dushman equation, $J_{A,S} = A_A T_A^2 exp[-q\Phi_A/(kT_A)]$. Here, $J_{A,S}$ is the saturation anode reverse current density, T_A is the anode temperature, k is the Boltzmann constant, and q is the electron charge.

Figure 4 shows characteristic comparisons of voltage and current density between the TI and the TIPV converters, respectively. It can be observed that the open-circuit voltage U_{open} is increased from ∼0.9 V of the TI converter to ∼1.9 V of the TIPV converter due to PV effect. The MPP voltage of all the converters increases as the cathode temperature rises. The U_{MPP} enhancement in Figure 4C refers to the MPP voltage of TIPV converter minus that of the TI converter. The U_{MPP} enhancement also shows an increasing trend as the
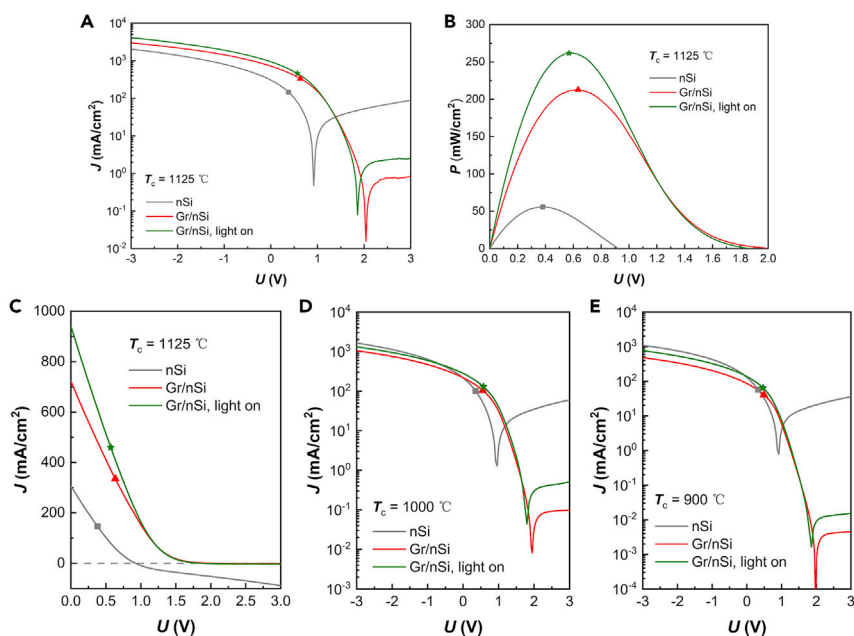
Figure 3. Experimental results of *J-U* and *P-U* relations of the TI and the TIPV converters

(A), (C) The *J-U* and (B) the *P-U* relations at the cathode temperature of 1125°C. The *J-U* relations at the cathode temperatures of (D) 1000°C and (E) 900°C, respectively. In panels (A), (D), and (E), *J* is in absolute value and on logarithmic axis. The symbol on curves represents the maximum power point (MPP). The devices generate power for positive U_{out} and consume energy for negative U_{out}. *J* is calculated via dividing current by the cathode-emitting area.

cathode temperature increases. The U_{MPP} of the TIPV and of the TI converters is 0.63 and 0.40 V, respectively, at the cathode temperature of 1150°C, resulting an enhancement of 0.23 V. At the temperature range of 800°C–975°C, both the short-circuit current density J_{short} and the MPP current density J_{MPP} of the TIPV converter are slightly lower than that of the TI converter. This is caused by insufficient photons for generating PV current. As the cathode temperature continues to rise, the corresponding current densities of the TIPV converter gradually exceed that of the TI converter. The J_{MPP} of the TIPV converter is ~3-fold than that of the TI converter at the cathode temperature of 1150°C Figure 5B shows the output power density as a function of the cathode temperature for converters of the TI, the TIPV, and the TIPV with illumination, respectively. The trend of the output power density is very close to that of the current density. With xenon lamp illumination on the anode, the PV current is further increased, leading to a further enhancement for the power density. The *J-U* and *P-U* relations with xenon lamp illumination are shown by the green lines in Figure 3. With illumination, the reverse current increases due to increased anode temperature and possibly existing photon-enhanced thermionic emission (Schwede et al., 2010; Qiu et al., 2022), especially at large voltage. Thus, both U_{MPP} and U_{open} are therefore penalized overall.

Saturation current of cathode is measured for the TIPV converter, and the corresponding Richardson constant A_C is taken as 70 A/(cm^2·K^2). Therefore, the work function of the cathode Φ_C (see Figure 5A) can be obtained according to the Richardson-Dushman equation, $J_S = A_C T_C^2 exp[- q\Phi_C/(kT_C)]$. Here, *k* is the Boltzmann constant and *q* is the electron charge. The cathode work function increases monotonically as the cathode temperature is raised. This also implies the anode work function is much lower than 2 eV. An electronic efficiency ηe can be calculated to qualitatively compare the performance of the converters. Electronic efficiency is defined as the ratio of P_{max} to the corresponding energy density Q_e taken away from the cathode by the emitted electrons. Q_e can be calculated by $Q_e = J_{MPP}/q \times (\psi_M + 2kT_C)$. Here, ψ_M is the maximum electron barrier in the electrode gap, and is approximated by the cathode work function Φ_C. Note that the electronic efficiency is distinct from the thermodynamic efficiency that accounts for the total heat input to the converters. In a practical device, the comprehensive performance should be evaluated on a thermodynamic efficiency basis.

Figure 5C shows the electronic efficiency of the TI and the TIPV converters, respectively, as a function of the cathode temperature. Both the output power density and the electronic efficiency of the TIPV converter are
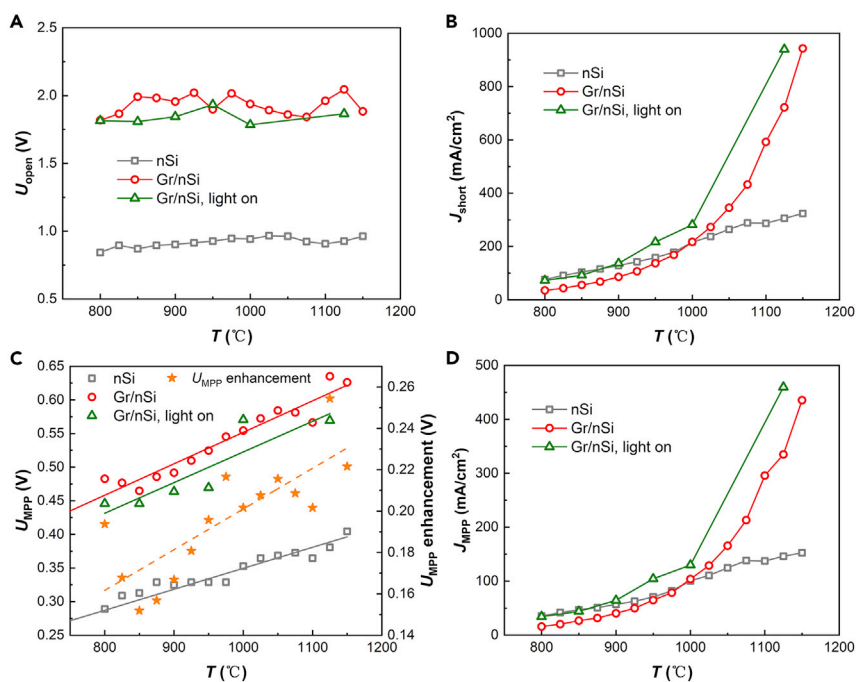
Figure 4. Characteristic comparisons between the TI and the TIPV converters

(A) U_{open}, (B) J_{short}, (C) U_{MPP}, and (D) J_{MPP} as functions of the cathode temperature. The U_{open} is approximately obtained at current density of 1×10^{-6} A/cm^2.

significantly enhanced compared with the TI one by the photovoltaic effect. At the cathode temperature of 1150°C, the output power of the TIPV converter reaches 272.8 mW/cm^2, which is 4.4 times higher than that of the TI one. The electron efficiency of the TIPV converter is increased to 26.5%, which is 9.4% higher than that of TI one. In order to verify that the enhancement is contributed by the aforementioned PV mechanism, rather than only by graphene layer, a TI converter with anode of single-layer graphene on copper substrate was also measured (see Figure S5). The graphene-on-copper anode TI converter behaves poor performance, which indicates that the enhancement is not contributed by the graphene layer.

In order to further illustrate the superiority of the TIPV converter, Figure 6 shows the comparison of the output power density between the TIPV converter and those reported in the literature. The results demonstrate that the output power density of the present TIPV converter is almost the leading in the studied temperature range. The output power densities for I (Campbell et al., 2020) and J (Beggs, 1963) are larger than that of this work, due to advantages such as smaller electrode gap size. It should be noted that our TIPV converter, as a proof-of-concept prototype, can also achieve a substantial improvement in performance, by measures such as further reducing the electrode gap size.

Figure 7 shows the working characteristics of the cathode temperatures of 1000°C and 1100°C, respectively, as a function of the interelectrode gap size. The J-U and the P-U relations can be found in Figure S7. The output power density for 1100°C is attenuated by more than two orders of magnitude (from 167.6 to 0.34 mA/cm^2) as the gap size increases from 30 to 900 μm. This penalization is caused by space charge effect. It is also observed that U_{open} gradually increases with the gap size, from 1.96 at 30 μm to 2.38 V at 900 μm for 1100°C. Since the TI current decreases, the operating point of the PV cell is biased toward its own open-circuit voltage, which increases the voltage enhancement. Therefore, the TIPV output voltage increases. This implies that TIPV converter can compensate for the penalization of space charge to a small extent in the form of increasing the output voltage compared with TI converter. The U_{MPP} and J_{MPP} variation trends with the interelectrode gap size can be found in Figure S8.

In far-field scenarios, photons are mainly absorbed by the semiconductor; only photons with energy larger than bandgap E_g contribute to PV current as described in the section of Concept and working principle. Lack of high-frequency thermal photons ($h\omega > E_g$, being h the Planck constant divided by 2π and ω the
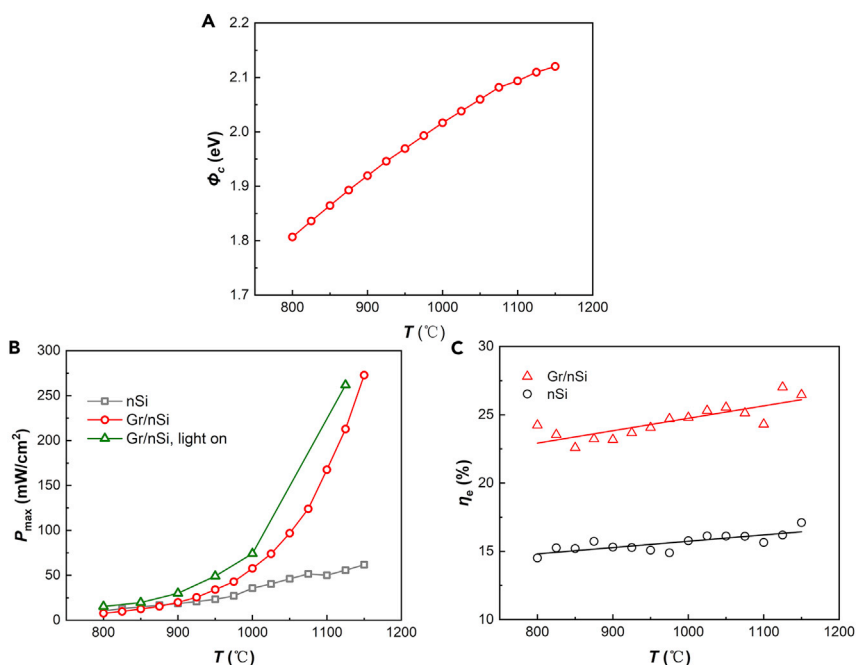
Figure 5. Performance trends of the TI and the TIPV converters as a function of the cathode temperature
(A) The cathode work function. Comparisons of (B) P_{max} and (C) η_e between the TI and the TIPV converters.

photon frequency) limits the current and potentiality of the TIPV converter with a graphene-on-semiconductor anode. A near-field configuration is an extremely promising scenario. With graphene plasmon polariton, photons can be resonantly absorbed in the graphene layer and the evanescent wave photon tunneling is significantly enhanced (Yang et al., 2018). In this case, the working principle of graphene-on-silicon PV cell is transformed into hot-electron mode, and photons with energy superior to the Schottky barrier height Φ_{SBH} can excite electrons of graphene layer over the barrier, thus generating photocurrent (St-Gelais et al., 2017; Yang et al., 2018). A graphene-on-silicon PV cell can yield an electrical power output of >1 × 10^5 W/m² at the radiator temperature of 700°C as previously reported (Yang et al., 2018). The tunable Φ_{SBH} reduces the difficulty of matching the TI and the PV currents near their respective MPPs to a certain extent by reasonably design. Meanwhile, a near-field gap size can eradicate the penalization by space charge effect. Compared with narrow bandgap semiconductors (e.g., InGaAs and InSb), graphene-on-semiconductor PV cell has the advantages of simple fabrication, low cost, graphene's tunable Fermi level, and strong infrared plasmonic response.

Limitations of the study

Barium adsorption property on the surface of the silicon anode and the graphene-on-silicon anode may be different, which in turn affects the formation of surface dipoles. This may lead to a lower work function of graphene-on-silicon than that of silicon. Thus, the reported significant advantage of the TIPV converter might due to a combined effect, rather than only contributed by the photovoltaic effect. In future work, other efficient cathodes that cannot contribute to the anode work function should be used for further study of TIPV converters with graphene-on-semiconductor anodes. In this way, the contribution from the photovoltaic effect can be shown more clearly.

In addition, the converters can maintain stable working performance after about 8 h of operation during the experiment. However, we have not conducted research on the long-term operation of the device in this work. A practical electricity generation device should operate stably for several months or even years. Thus, device lifetime and stability are meaningful for future research.

Conclusion

In summary, we have proposed a TIPV converter with graphene-on-semiconductor heterojunction anode and conducted the first proof-of-concept demonstration. On the one hand, the unexpected SPV effect
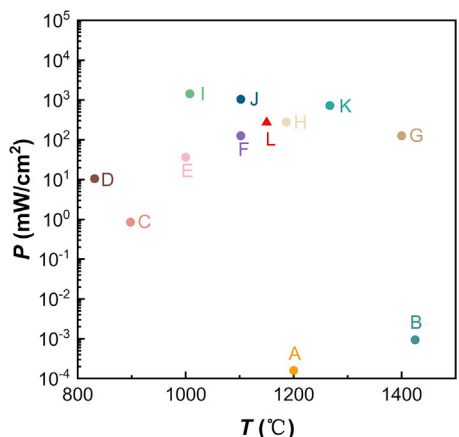
Figure 6. Reported power density of TI converters in the literature

This has been refined on the basis of the literature (Campbell et al., 2021). The letters refer to the references at the end of this article, except for L that denotes results of this study. Note that the power density of this work was calculated on the cathode emitting area basis, and that the anode area is ~7-fold larger than that of the cathode. A (Bellucci et al., 2022b), B (Bellucci et al., 2020), C (King et al., 2001), D (Belbachir et al., 2014), E (Yuan et al., 2017), F (Meir et al., 2013), G (Bellucci et al., 2022a), H (Littau et al., 2013), I (Campbell et al., 2020), J (Beggs, 1963), and K (Hatsopoulos and Kaye, 1958).

of p-type III-V semiconductor in typical TIPV converters is eliminated. On the other hand, it takes the merits of graphene-on-silicon PV cell, i.e., easy fabrication, low cost, graphene plasmon polariton in near-field scenario, and tunable properties. We demonstrated a substantial U_{open} boost from 0.9 to 1.9 V by comparing with an identical configuration without graphene layer. A power density of 2.7 kW/m^2 with an electronic efficiency of ~27% was measured at the cathode temperature of 1150°C and at the interelectrode gap size of ~30 μm. In the prototype, a dispenser cathode was manufactured with a work function ranging from 1.8 to 2.12 eV. The anode surface was also engineered by barium layer to gain a work function much lower than 2 eV. Experiment also demonstrates that TIPV can compensate for the penalization caused by space charge in a small range. In addition, the TIPV converter with near-field interelectrode gap size has a promising prospect. This is due to substantial super-Planckian photon tunneling by graphene plasmon polariton, working principle of hot-carrier-based PV cells, and circumvent of space charge limitation.

STAR★METHODS

Detailed methods are provided in the online version of this paper and include the following:

- KEY RESOURCES TABLE
- RESOURCE AVAILABILITY
  - Lead contact
  - Materials availability
  - Data and code availability
- METHOD DETAILS
  - Measurement method
  - Sample preparation
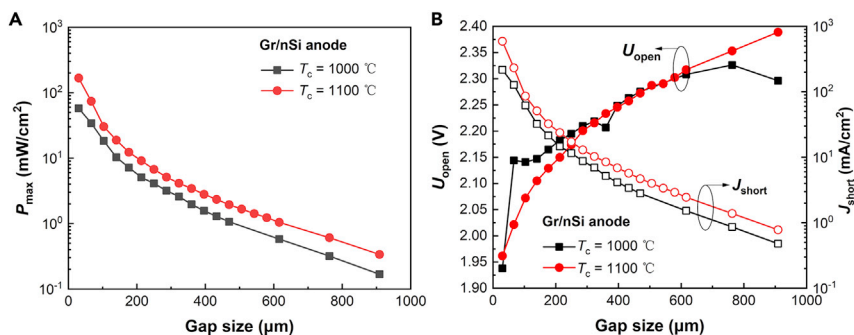 - Physical characterization

Figure 7. Performance of the TIPV converter as functions of the interelectrode gap size

(A) P_{max}. (B) U_{open} and J_{short}. The black and red colors correspond to the cathode temperature of 1000°C and 1100°C, respectively.

CellPress
OPEN ACCESS

AUTHOR CONTRIBUTIONS

Conceptualization, H.Q.; Methodology, H.Q.; Investigation, H.Q.; Resources, H.Q., S.L., and G.H.; Formal Analysis, H.Q.; Visualization, H.Q.; Writing - Original Draft, H.Q.; Writing - Review & Editing, H.Q., H.X., S.L., and G.X.; Supervision, G.X.; Project Administration, G.X.; Funding Acquisition, G.X.

DECLARATION OF INTERESTS

The authors declare no competing interests.

REFERENCES

Beggs, J.E. (1963). Vacuum thermionic energy converter. Adv. Energy Convers. *3*, 447–453. https://doi.org/10.1016/0365-1789(63)90062-6.

Belbachir, R.Y., An, Z., and Ono, T. (2014). Thermal investigation of a micro-gap thermionic power generator. J. Micromech. Microeng. *24*, 085009. https://doi.org/10.1088/0960-1317/24/8/085009.

Bellucci, A., García-Linares, P., Martí, A., Trucchi, D.M., and Datas, A. (2022). A three-terminal hybrid thermionic-photovoltaic energy converter. Adv. Energy Mater. *12*, 2200357. https://doi.org/10.1002/aenm.202200357.

Bellucci, A., Linares, P.G., Villa, J., Martí, A., Datas, A., and Trucchi, D.M. (2022b). Hybrid thermionic-photovoltaic converter with an In0.53Ga0.47As anode. Sol. Energy Mater. Sol. Cells *238*, 111588. https://doi.org/10.1016/j.solmat.2022.111588.

Bellucci, A., Mastellone, M., Orlando, S., Girolami, M., Generosi, A., Paci, B., Soltani, P., Mezzi, A., Kaciulis, S., Polini, R., and Trucchi, D.M. (2019). Lanthanum (oxy)boride thin films for thermionic emission applications. Appl. Surf. Sci. *479*, 296–302. https://doi.org/10.1016/j.apsusc.2019.01.230.

Bellucci, A., Mastellone, M., Serpente, V., Girolami, M., Kaciulis, S., Mezzi, A., Trucchi, D.M., Antolín, E., Villa, J., Linares, P.G., et al. (2020). Photovoltaic anodes for enhanced thermionic energy conversion. ACS Energy Lett. *5*, 1364–1370. https://doi.org/10.1021/acsenergylett.0c00022.

Bennett, G.L., Hemler, R.J., and Schock, A. (1996). Space nuclear power - an overview. J. Propuls. Power *12*, 901–910. https://doi.org/10.2514/3.24121.

Campbell, M.F., Azadi, M., Lu, Z., Eskenazi, A.G., Jain, A., Bang, J.W., Sieg, P.G., Popov, G.A., Nicaise, S.M., Van Houten, K.C., et al. (2020). Nanostructured Spacers for thermionic and thermophotovoltaic energy converters. J. Microelectromech. Syst. *29*, 637–644. https://doi.org/10.1109/JMEMS.2020.3000422.

Campbell, M.F., Celenza, T.J., Schmitt, F., Schwede, J.W., and Bargatin, I. (2021). Progress toward high power output in thermionic energy converters. Adv. Sci. *8*, 2003812. https://doi.org/10.1002/advs.202003812.

Datas, A., and Vaillon, R. (2019a). Thermionic-enhanced near-field thermophotovoltaics. Nano Energy *61*, 10–17. https://doi.org/10.1016/j.nanoen.2019.04.039.

Datas, A., and Vaillon, R. (2019b). Thermionic-enhanced near-field thermophotovoltaics for medium-grade heat sources. Appl. Phys. Lett. *114*, 133501. https://doi.org/10.1063/1.5078602.

Deng, Y., Qiu, B., Yin, Y., Wu, Y., and Su, G. (2021). Design and evaluation of a high power density and high energy efficiency fuel element for space nuclear reactors. Appl. Therm. Eng. *191*, 116915. https://doi.org/10.1016/j.applthermaleng.2021.116915.

Forman, R. (1976). Surface studies of barium and barium oxide on tungsten and its application to understanding the mechanism of operation of an impregnated tungsten cathode. J. Appl. Phys. *47*, 5272–5279. https://doi.org/10.1063/1.322602.

Hatsopoulos, G.N., and Kaye, J. (1958). Measured thermal Efficiencies of a Diode configuration of a thermo electron engine. J. Appl. Phys. *29*, 1124–1125. https://doi.org/10.1063/1.1723373.

King, D.B., Luke, J.R., and Zavadil, K.R. (2001). The microminiature thermionic converter. AIP Conf. Proc. *552*, 1152–1157. https://doi.org/10.1063/1.1358065.

Koeck, F.A.M., and Nemanich, R.J. (2017). Advances in thermionic energy conversion through single-Crystal n-type diamond. Front. Mech. Eng. *3*, 00019. https://doi.org/10.3389/fmech.2017.00019.

Kong, X., Zhang, L., Liu, B., Gao, H., Zhang, Y., Yan, H., and Song, X. (2019). Graphene/Si Schottky solar cells: a review of recent advances and prospects. RSC Adv. *9*, 863–877. https://doi.org/10.1039/C8RA08035F.

Li, X., Zhu, H., Wang, K., Cao, A., Wei, J., Li, C., Jia, Y., Li, Z., Li, X., and Wu, D. (2010). Graphene-on-silicon Schottky junction solar cells. Adv. Mater. *22*, 2743–2748. https://doi.org/10.1002/adma.200904383.

Lin, S.-S., Wu, Z.-Q., Li, X.-Q., Zhang, Y.-J., Zhang, S.-J., Wang, P., Panneerselvam, R., and Li, J.-F. (2016). Stable 16.2% efficient surface plasmon-enhanced graphene/GaAs Heterostructure solar cell. Adv. Energy Mater. *6*, 1600822. https://doi.org/10.1002/aenm.201600822.

Littau, K.A., Sahasrabuddhe, K., Barfield, D., Yuan, H., Shen, Z.-X., Howe, R.T., and Melosh, N.A. (2013). Microbead-separated thermionic energy converter with enhanced emission current. Phys. Chem. Chem. Phys. *15*, 14442–14446. https://doi.org/10.1039/C3CP52895B.

Meir, S., Stephanos, C., Geballe, T.H., and Mannhart, J. (2013). Highly-efficient thermoelectronic conversion of solar energy and heat into electric power. Journal of Renewable and Sustainable Energy *5*, 043127. https://doi.org/10.1063/1.4817730.

Rahman, E., and Nojeh, A. (2021). Semiconductor thermionics for next generation solar cells: photon enhanced or pure thermionic? Nat. Commun. *12*, 4622. https://doi.org/10.1038/s41467-021-24891-2.

Qiu, H., Xu, H., Ni, M., and Xiao, G. (2022). Photo-thermo-electric modeling of photon-enhanced thermionic emission with concentrated solar power. Sol. Energy Mater. Sol. Cell. *246*, 111922. https://doi.org/10.1016/j.solmat.2022.111922.

Schindler, P., Riley, D.C., Bargatin, I., Sahasrabuddhe, K., Schwede, J.W., Sun, S., Pianetta, P., Shen, Z.-X., Howe, R.T., and Melosh, N.A. (2019). Surface photovoltage-induced ultralow work function material for thermionic energy converters. ACS Energy Lett. 4, 2436–2443. https://doi.org/10.1021/acsenergylett.9b01214.

Schwede, J.W., Bargatin, I., Riley, D.C., Hardin, B.E., Rosenthal, S.J., Sun, Y., Schmitt, F., Pianetta, P., Howe, R.T., Shen, Z.X., and Melosh, N.A. (2010). Photon-enhanced thermionic emission for solar concentrator systems. Nat. Mater. 9, 762–767. https://doi.org/10.1038/nmat2814.

Schwede, J.W., Sarmiento, T., Narasimhan, V.K., Rosenthal, S.J., Riley, D.C., Schmitt, F., Bargatin, I., Sahasrabuddhe, K., Howe, R.T., Harris, J.S., et al. (2013). Photon-enhanced thermionic emission from heterostructures with low interface recombination. Nat. Commun. 4, 1576. https://doi.org/10.1038/ncomms2577.

Serpente, V., Bellucci, A., Girolami, M., Mastellone, M., Mezzi, A., Kaciulis, S., Carducci, R., Polini, R., Valentini, V., and Trucchi, D.M. (2020). Ultra-thin films of barium fluoride with low work function for thermionic-thermophotovoltaic applications. Mater. Chem. Phys. 249, 122989. https://doi.org/10.1016/j.matchemphys.2020.122989.

St-Gelais, R., Bhatt, G.R., Zhu, L., Fan, S., and Lipson, M. (2017). Hot carrier-based near-field thermophotovoltaic energy conversion. ACS Nano 11, 3001–3009. https://doi.org/10.1021/acsnano.6b08597.

Sun, M., Tang, W., Ren, Q., Wang, S., JinYu Du, Y., Du, Y., and Zhang, Y. (2015). First-principles study of the alkali earth metal atoms adsorption on graphene. Appl. Surf. Sci. 356, 668–673. https://doi.org/10.1016/j.apsusc.2015.08.102.

Trucchi, D.M., Bellucci, A., Girolami, M., Calvani, P., Cappelli, E., Orlando, S., Polini, R., Silvestroni, L., Sciti, D., and Kribus, A. (2018). Solar thermionic-Thermoelectric generator (ST2G): concept, materials engineering, and prototype demonstration. Adv. Energy Mater. 8, 1802310. https://doi.org/10.1002/aenm.201802310.

Xiao, G., Zheng, G., Qiu, M., Li, Q., Li, D., and Ni, M. (2017). Thermionic energy conversion for concentrating solar power. Appl. Energy 208, 1318–1342. https://doi.org/10.1016/j.apenergy.2017.09.021.

Yang, J., Du, W., Su, Y., Fu, Y., Gong, S., He, S., and Ma, Y. (2018). Observing of the super-Planckian near-field thermal radiation between graphene sheets. Nat. Commun. 9, 4033. https://doi.org/10.1038/s41467-018-06163-8.

Yuan, H., Chang, S., Bargatin, I., Wang, N.C., Riley, D.C., Wang, H., Schwede, J.W., Provine, J., Pop, E., Shen, Z.-X., et al. (2015). Engineering ultra-low work function of graphene. Nano Lett. 15, 6475–6480. https://doi.org/10.1021/acs.nanolett.5b01916.

Yuan, H., Riley, D.C., Shen, Z.X., Pianetta, P.A., Melosh, N.A., and Howe, R.T. (2017). Back-gated graphene anode for more efficient thermionic energy converters. Nano Energy 32, 67–72. https://doi.org/10.1016/j.nanoen.2016.12.027.

STAR★METHODS

KEY RESOURCES TABLE

REAGENT or RESOURCE	SOURCE	IDENTIFIER
Other		
CVD monolayer graphene	XFNANO Mater Tech Co., Ltd, China	N/A
Silicon wafer	Shanghai Institute of Optics and Fine Mechanics, Chinese Academy of Sciences	N/A
Scanning electron microscopy	Hitachi	SU3800
X-ray diffraction spectrum	Rigaku	D/max 2550 PC
Atomic force microscopy	Bruker	Dimension Icon
Current-voltage acquisition instrument	Keithley	B2901A
Infrared thermometer	IMPAC	IGA-140

RESOURCE AVAILABILITY

Lead contact

Further information and requests for resources and reagents should be directed to and will be fulfilled by the Lead Contact, Gang Xiao (xiaogangtianmen@zju.edu.cn).

Materials availability

This study did not generate new unique reagents.

Data and code availability

- All data reported in this paper will be shared by the lead contact upon request.

- This study did not report original code.

- Any additional information required to reanalyze the data reported in this work paper is available from the lead contact upon request.

METHOD DETAILS

Measurement method

For measurements of both the TI and the TIPV prototypes, a custom high-vacuum experiment system was developed, as the schematic shown in Figure 2A. The cathode and anode of prototypes were sealed in a custom high-vacuum chamber. Vacuum conditions ($<10^{-5}$ Pa) were maintained by a dry scroll vacuum pump (Agilent IDP 7) and a turbo molecular pump (Agilent TwisTorr 304 FS). Vacuum condition was monitored by a compound vacuum gauge (ZDF-5201AXv01 produced by Chengdu Ruibao Co., Ltd.) with an ionization vacuum gauge (ZJ-12 produced by Chengdu Ruibao Co., Ltd.). For the assembly of electrodes, anode was mounted on a 5-axis manipulator with a 2.93 μm translational precision and the cathode was stationary. The distance between cathode and anode was adjusted by the manipulator. Due to thermal bowing or stretching of the materials, we have to calibrate the distance at each temperature. In this process, we observe the current of the prototypes while fine-tuning the gap size. The current increases significantly and instantaneously when the cathode and anode just touch. We take this state as zero gap size, and then quickly adjust to the target gap size. For the anode illumination, the light source was provided by a xenon lamp with spectral range of 250-1200 nm and electric power of about 500 W.

We used a Keithley B2901A system source meter measure current-voltage curves of the TI and the TIPV converters. The cathode temperature was measured by an infrared thermometer (IMPAC IGA-140) through a quartz viewing window. The infrared thermometer measurement was confirmed by a K-type thermocouple at a temperature range of 200-450°C. The average relative deviation of the two methods is 10.6%, which is acceptable for our experiment. Comparison of cathode temperature measured by the two methods is shown in Figure S9. The inside of the dispenser cathode is filled with aluminum oxide

and a tungsten-rhenium alloy wire for electric heating. The electricity was provided by an adjustable DC power supply. In this way, the cathode can be heated to and stabilized at given any temperature in the range of 100-1200°C. We cannot accurately measure the anode temperature in our experiment, but we arranged a K-type thermocouple near the anode. The measured temperature of the thermocouple is shown in Figure S10.

Sample preparation

In the measurement, we used a dispenser cathode and a graphene-on-silicon heterojunction anode. The dispenser cathode was manufactured with 3 mm diameter and 10 mm length. A porous tungsten matrix was impregnated with active materials (i.e., barium-calcium aluminate, see Figure S1). Then a thin film of osmium (Os) was coated on the emitting surface. The polished silicon wafer doped with phosphorus ($1\text{-}2 \times 10^{18}$ cm^{-3}) was used to fabricate graphene-on-silicon heterojunction. Mono-layer graphene was grown on copper foil by chemical vapor deposition (CVD) and then was transferred to the silicon surface by a standard polymethyl methacrylate (PMMA) mediated method, forming a Schottky junction at the interface. Graphene side was spin-coated with PMMA as support layer for transferring and then the PMMA layer was removed by acetone. Sample characterizations can be found in Figures S1–S3.

Physical characterization

Scanning electron microscopy (SEM) with energy dispersive spectra (EDS) was measured by a field emission scanning electron microscope (Hitachi SEM SU3800). X-ray diffraction spectrum of aluminate for impregnating dispenser cathodes was measured by a polycrystalline diffractometer (Rigaku D/max 2550 PC). For the characterization of atomic force microscopy (AFM), a Bruker Dimension Icon AFM equipment was used. Raman spectrum was measured by a Renishaw inVia system.